Technical University of Denmark

DTU

An efficient and accurate method for computation of energy release rates in beam structures with longitudinal cracks

Blasques, José Pedro Albergaria Amaral; Bitsche, Robert

DTU Library
Technical Information Center of Denmark

An efficient and accurate method for computation of energy release rates in beam structures with longitudinal cracks

J. P. Blasques, R. D. Bitsche[*]

Department of Wind Energy, Technical University of Denmark, Frederiksborgvej 399, 4000 Roskilde, Denmark

Abstract

This paper proposes a novel, efficient, and accurate framework for fracture analysis of beam structures with longitudinal cracks. The three-dimensional local stress field is determined using a high-fidelity beam model incorporating a finite element based cross section analysis tool. The Virtual Crack Closure Technique is used for computation of strain energy release rates. The devised framework was employed for analysis of cracks in beams with different cross section geometries. The results show that the accuracy of the proposed method is comparable to that of conventional three-dimensional solid finite element models while using only a fraction of the computation time.

Keywords: Beam finite element, Beam cross section analysis, Energy release rate, Virtual crack closure technique, Longitudinal cracks in beams

Nomenclature

a	Element length next to the crack tip.
a_1, a_2	Element length behind and in front of crack tip, respectively.
c	Element width at crack front.
E_α	Elastic modulus of material α.
$\hat{\mathbf{f}}, \hat{\mathbf{f}}_e$	Global and element load vector for beam finite element model.
$\bar{\mathbf{f}}, \bar{\mathbf{f}}_e$	Global and element load vector for 3D solid finite element model.
$\mathbf{f}, \mathbf{f}_e$	Global and element load vector for cross section finite element model.
$\mathbf{F}_s$	Cross section compliance matrix.
$G_{I,II,III}$	Mode-I, II, and III energy release rates.
H	Height of the square cross section.
K_{III}	Mode-III stress intensity factor.
$\hat{\mathbf{K}}, \hat{\mathbf{K}}_e$	Global and element stiffness matrix for beam finite element model.
$\bar{\mathbf{K}}, \bar{\mathbf{K}}_e$	Global and element stiffness matrix for 3D solid finite element model.
$\mathbf{K}, \mathbf{K}_e$	Global and element stiffness matrix for cross section finite element model.
$\mathbf{K}_s$	Cross section stiffness matrix.
L_0	Reference evaluation distance for the mode mixity.
L_e	Length of beam finite element e.
$M_{x,y,z}$	Cross section moments around the x, y and z axis.
n_b	Number of beam elements in the beam finite element assembly.
n_s	Number of beam elements in the solid finite element assembly.
$\hat{\mathbf{r}}_e$	Element internal reaction forces at beam finite element e.
$\bar{\mathbf{r}}_e$	Element internal reaction forces at 3D solid finite element e.

[*]Corresponding author

Email addresses: `jpbl@dtu.dk` (J. P. Blasques), `robi@dtu.dk` (R. D. Bitsche)

$\mathbf{r}_e$	Element internal reaction forces at cross section finite element e.
r	Distance from the crack tip.
$r_i^{1,2,3}$	Nodal force at the crack tip in the x_1, x_2 and x_3 direction at node i.
$\mathbf{s}$	Total displacement of a point in the beam cross section.
$T_{x,y,z}$	Cross section forces in the x, y and z directions of the cross section coordinate system.
$\mathbf{u}$	Displacement of a point in the beam cross section due to warping deformation.
$\hat{\mathbf{u}}, \hat{\mathbf{u}}_e$	Global and element displacement vector for beam finite element model.
$\overline{\mathbf{u}}, \overline{\mathbf{u}}_e$	Global and element displacement vector for 3D solid finite element model.
$u_i^{1,2,3}$	Nodal displacement at node i in the x_1, x_2 and x_3 directions of the crack coordinate system.
$\Delta u_{i,j}^{1,2,3}$	Relative nodal displacements between node i and j in the x_1, x_2 and x_3 directions of the crack coordinate system.
$\mathbf{v}$	Displacement of a point in the beam cross section due to rigid body motion.
$\mathbf{w}, \mathbf{w}_e$	Global and element displacement vector for cross section finite element model.
W	Width of the square cross section.
x, y, z	Axes of the cross section coordinate system.
X, Y, Z	Axes of the global coordinate system.
x_1, x_2, x_3	Axes of the crack coordinate system.
β	Second Dundurs parameter.
η	Bi-material constant.
$\boldsymbol{\theta}$	Cross section forces and moments.
$\kappa_{x,y,z}$	Cross section curvatures around the x, y and z directions of the cross section coordinate system.
κ_α	Generalized plane stress material parameter of material α.
μ_α	Shear modulus of material α.
ν_α	Poisson's ratio of material α.
$\tau_{x,y,z}$	Cross section shear strains in the xz (τ_x) and yz (τ_y) planes, and normal strain in the z direction (τ_z) according to the cross section coordinate system.
ψ	Mode mixity angle.
$\boldsymbol{\psi}$	Cross section strains and curvatures.
$\hat{()}$	Quantities associated with the beam finite element model.
$\overline{()}$	Quantities associated with the 3D solid finite element model.
BECAS	BEam Cross section Analysis Software.
ERR	Energy Release Rate.
FE	Finite Element.
VCCT	Virtual Crack Closure Technique.

1. Introduction

This work is motivated by the challenges associated with the analysis of cracks in wind turbine rotor blades. The structural analysis of blades is typically performed in a finite element context. For example, Overgaard and Lund [16], Overgaard et al. [17], and Overgaard et al. [18] presented a solid and shell finite element model for simulating the collapse of a wind turbine blade under static loading. The fracture analysis is based on the cohesive element approach (Barenblatt [2]). More recently, Eder and Bitsche [9] presented a similar modeling approach using the Virtual Crack Closure Technique (VCCT) for the analysis of cracks in trailing edge adhesive joints of a wind turbine rotor blade. The present paper introduces a novel modeling approach combining a finite element based cross section analysis tool and VCCT.

The VCCT is a well established method for the computation of the energy release rate (ERR) based on results from finite element analysis (Rybicki and Kanninen [20], Xie and Waas [22], and Krueger [12] and references therein). The VCCT is computationally efficient and provides the modal contributions to the total ERR, where the latter is crucial for mixed mode fracture analysis. This technique is based on linear elastic fracture mechanics and on the assumption that the energy released during crack propagation equals the work required to close the crack back to its original position. Based on this assumption, the ERR is computed from the nodal forces at the crack tip and relative nodal displacements
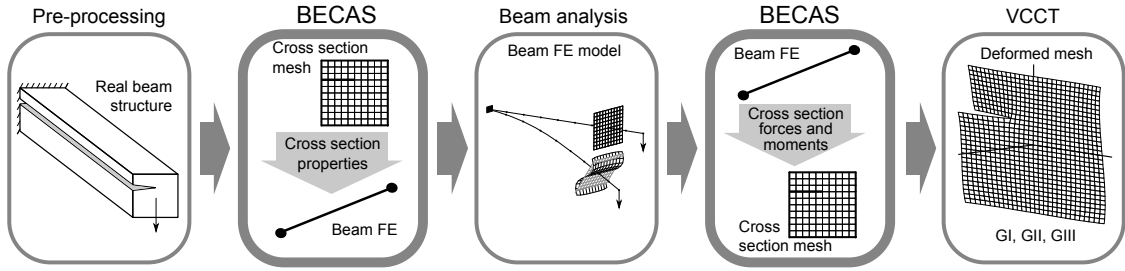
Figure 1: Schematic description of proposed computational workflow based on a high-fidelity beam finite element model for analysis of beams featuring a crack that extends along its length.

behind the crack tip. The finite element models providing the required nodal forces and nodal displacements are typically based on plane stress or strain, shell, or solid finite elements (see Krueger [12] for an extensive review on the topic). As a relatively fine mesh must be used in the area surrounding the crack, three-dimensional models of this kind are often computationally expensive. This is especially true if the location, orientation and size of the crack is not known *a priori*, and a large number of model configurations must be analyzed.

In this paper an efficient framework is proposed for the computation of all three components of the ERR. The method is applicable to beam structures featuring a crack that extends along the length of the structure, as shown in Fig. 1. In engineering practice a crack that does not extend along the entire length of the beam, can often conservatively be assumed to do so. The structural response of the beam is analyzed using a high-fidelity beam model. This model is composed of two parts – a 2D cross section analysis tool and 3D beam finite element model. The workflow used in this paper comprises three steps. The first step entails the accurate determination of the cross section stiffness properties. This is done using the BEam Cross section Analysis Software – BECAS[1] – an implementation by Blasques and Stolpe [5] and Blasques [4] of the theory originally presented by Giavotto et al. [10]. This tool relies on a 2D finite element discretization of the beam cross section geometry to accurately compute its stiffness properties. BECAS can correctly handle sections of arbitrary geometry and account for effects of material anisotropy and inhomogeneity. The reader is referred to Volovoi et al. [21] for a comprehensive assessment of different cross section modeling techniques. In the second step, the cross section stiffness properties are integrated along the length of the beam to generate the 3D beam finite element stiffness matrices. The resulting cross section and beam finite element matrices are significantly smaller and therefore computationally faster to evaluate rendering this modeling approach an efficient alternative to shell or solid finite element models. The proposed model is suited for the analysis of long slender beam-like structures presenting a certain degree of lengthwise continuity of the loads, geometry, and material properties, e.g., a wind turbine rotor blade. In the third and last step, the cross section forces and moments at the section of interest are determined for a given load case from the beam finite element equations. These are used again in BECAS to determine the nodal displacements and nodal reaction forces in the cross section finite element mesh, namely, at the crack tip. The resulting values are then used within the VCCT framework to determine the ERR.

Note that the analysis problem has two length scales – a beam scale associated with the length dimension of the beam and a cross section scale associated with the cross section dimensions. At the beam scale the numerical model proposed in this paper can be used to evaluate the global static and dynamic response with accuracy comparable to that of 3D finite element models. At the cross section scale the results – e.g., local stresses or strain energy release rates – are only a function of the cross section forces and moments. Hence, these results may not be as accurate as results obtained from 3D finite element models in regions, e.g., where concentrated loads are applied or close to boundary conditions where in- and out-of-plane cross section deformation is restrained. For the examples investigate in this paper the accuracy of this approach is comparable to that of computationally more expensive 3D finite element models. To the authors' best knowledge this represents a novel approach in numerical fracture analysis.

This paper is structured as follows. The structural model is described first in Section 2. The VCCT formulas specific for the described structural model are derived in Section 3. The proposed methodology is consequently demonstrated and validated for four numerical examples. The setup for these numerical experiments and all the

---

[1]BECAS is available as a Matlab[TM] source code. An academic license is available free of charge at www.becas.dtu.dk.

3

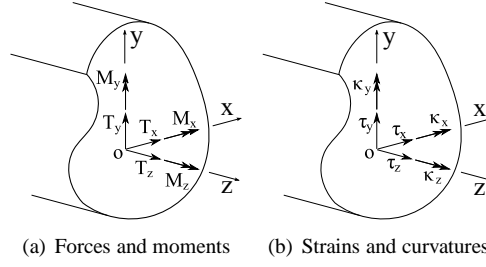(a) Forces and moments   (b) Strains and curvatures

Figure 2: Section coordinate system, cross section forces $\mathbf{T}$ and moments $\mathbf{M}$ (left), and corresponding strains $\boldsymbol{\tau}$ and curvatures $\boldsymbol{\kappa}$ (right) (from Blasques and Stolpe [5]).

relevant results are presented in Section 4. Finally, the results are discussed in Section 5 and the main conclusions are presented in Section 6.

2. Structural model

The structural response of the beam is analyzed using the beam model originally presented by Blasques and Stolpe [5]. The model is based on the assumptions that the material and geometrical properties present a certain degree of continuity along the length of the beam. The original beam structure is represented by a reference line defined along the length of the beam going through the reference points of a series of representative cross sections. The reference line is discretized using beam finite elements whose stiffness matrices result from the lengthwise integration of the cross section stiffness properties.

A brief presentation of the methodology employed in the estimation of the cross section stiffness properties is described first. The beam finite element equations are derived next. Only the most relevant steps of the derivations are presented here. The reader is referred to Blasques and Stolpe [5] for further details.

2.1. Cross section analysis

The cross section stiffness properties are described by the parameters contained in the 6×6 cross section stiffness matrix $\mathbf{K}_s$. This matrix establishes the relation between the section forces and moments in $\boldsymbol{\theta}$, and the strains and curvatures in $\boldsymbol{\psi}$ (see Fig. 2) through the cross section constitutive relation $\boldsymbol{\theta} = \mathbf{K}_s \boldsymbol{\psi}$. The components of the cross section forces and moments $\boldsymbol{\theta} = \begin{bmatrix} \mathbf{T}^T & \mathbf{M}^T \end{bmatrix}^T$ are the transverse forces T_x and T_y, and axial force T_z in $\mathbf{T} = \begin{bmatrix} T_x & T_y & T_z \end{bmatrix}^T$, and the bending moments M_x and M_y, and torsional moment M_z in $\mathbf{M} = \begin{bmatrix} M_x & M_y & M_z \end{bmatrix}^T$. The components of the generalized strain-curvature vector $\boldsymbol{\psi}^T = \begin{bmatrix} \boldsymbol{\tau}^T & \boldsymbol{\kappa}^T \end{bmatrix}^T$ are the shear strains τ_x and τ_y, and the axial strain τ_z in $\boldsymbol{\tau}$. The remaining components are the bending curvatures κ_x and κ_y, and the twist rate κ_z in $\boldsymbol{\kappa}$. The accuracy of the beam finite element model depends to a large extent on the ability to correctly predict $\mathbf{K}_s$. The high-fidelity general purpose cross section analysis technique originally presented by Giavotto et al. [10] and implemented by Blasques and Stolpe [5] addresses this challenge and is employed here.

Consider a beam structure deforming under a given external load (see Fig. 3). It is assumed that the total displacement of an arbitrary point in a cross section of the beam is described by the sum of two contributions. The first contribution consists of the displacements associated with the rigid body translations and rotations of a reference point in the cross section. The second contribution is associated with the displacements stemming from the in- and out-of-plane deformation of the cross section henceforth referred to as warping displacements. Giavotto et al. [10] proposed an approach based on this separation of the displacements for the derivation of the cross section equilibrium equations and consequently of the stiffness parameters in $\mathbf{K}_s$. The approach relies on a 2D finite element representation of the cross section geometry (see, e.g., Fig. 7). Two different element types are considered in this paper, namely, a linear four node element and a quadratic eight node element henceforth referred to as Q4 and Q8, respectively. The 3D material constitutive properties are defined at each element and may exhibit any degree of anisotropy. Each node of
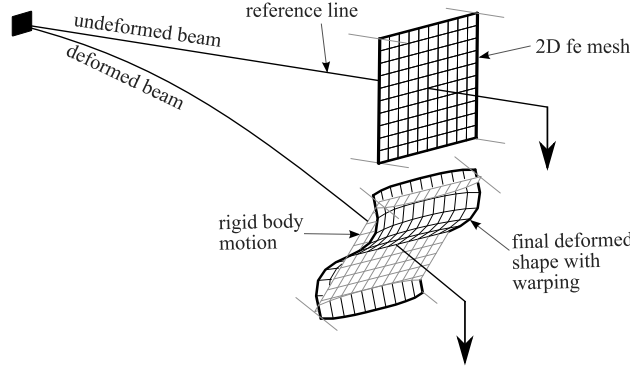
4

Figure 3: Schematic description of the deformation of a cantilever beam subjected to a tip load. The reference line is meshed using beam finite elements. The deformation of each cross section is described in terms of the rigid body motions and warping displacements. Cross section deformation is analysed using the cross section analysis tool BECAS where a finite element discretization of the cross section geometry is used to approximate the warping deformation.

the finite element mesh has three displacement degrees of freedom which approximate the 3D warping displacement field. The cross section equilibrium equations are then derived and given in matrix form (Blasques and Stolpe [5]) as

$$\mathbf{K}\mathbf{w} = \mathbf{f} \Leftrightarrow \begin{bmatrix} \mathbf{K}_{11} & \mathbf{K}_{12} \\ \mathbf{0} & \mathbf{K}_{11} \end{bmatrix} \begin{bmatrix} \mathbf{w}_1 \\ \mathbf{w}_2 \end{bmatrix} = \begin{bmatrix} \mathbf{f}_1 \\ \mathbf{f}_2 \end{bmatrix} \tag{1}$$

where the matrices $\mathbf{K}_{11}$ and $\mathbf{K}_{12}$ are defined in Blasques and Stolpe [5] and the solution vectors are $\mathbf{w}_1 = \begin{bmatrix} \mathbf{u}^T & \boldsymbol{\psi}^T & \lambda_1^T \end{bmatrix}^T$ and $\mathbf{w}_2 = \begin{bmatrix} \frac{\partial \mathbf{u}^T}{\partial z} & \frac{\partial \boldsymbol{\psi}^T}{\partial z} & \lambda_2^T \end{bmatrix}^T$. The components of the right hand-side vectors are $\mathbf{f}_1 = \begin{bmatrix} \mathbf{0} & \boldsymbol{\theta}^T & \mathbf{0} \end{bmatrix}^T$ and $\mathbf{f}_2 = \begin{bmatrix} \mathbf{0} & (\mathbf{T}_r\boldsymbol{\theta})^T & \mathbf{0} \end{bmatrix}^T$ where $\mathbf{T}_r\boldsymbol{\theta} = [0\ 0\ 0\ T_y\ -T_x\ 0]^T$. The Lagrange multipliers λ_1 and λ_2 are associated with the six constraints introduced to remove the rigid body motions from the warping displacements. The cross section equilibrium equations in (1) yield the warping displacements $\mathbf{u}$ and the generalized strains and curvatures $\boldsymbol{\psi}$ (associated with the rigid body translations and rotations) which balance the cross section forces and moments in $\boldsymbol{\theta}$.

The stiffness parameters in $\mathbf{K}_s$ can now be determined. First the cross section equilibrium equations in eq. (1) have to be solved for six unit load vectors $\boldsymbol{\theta}$ where each of the entries is set in turn to unity and the remaining to zero. This corresponds to solving the following linear system of equations

$$\mathbf{K}\mathbf{W} = \mathbf{F} \Leftrightarrow \begin{bmatrix} \mathbf{K}_{11} & \mathbf{K}_{12} \\ \mathbf{0} & \mathbf{K}_{11} \end{bmatrix} \begin{bmatrix} \mathbf{W}_1 \\ \mathbf{W}_2 \end{bmatrix} = \begin{bmatrix} \mathbf{F}_1 \\ \mathbf{F}_2 \end{bmatrix} \tag{2}$$

where $\mathbf{W}_1 = \begin{bmatrix} \mathbf{U}^T & \boldsymbol{\Psi}^T & \boldsymbol{\Lambda}_1^T \end{bmatrix}^T$, $\mathbf{W}_2 = \begin{bmatrix} \frac{\partial \mathbf{U}^T}{\partial z} & \frac{\partial \boldsymbol{\Psi}^T}{\partial z} & \boldsymbol{\Lambda}_2^T \end{bmatrix}^T$, $\mathbf{F}_1 = \begin{bmatrix} \mathbf{0}^T & \mathbf{I}_6 & \mathbf{0}^T \end{bmatrix}^T$, and $\mathbf{F}_2 = \begin{bmatrix} \mathbf{0}^T & \mathbf{T}_r & \mathbf{0}^T \end{bmatrix}^T$. Essentially, eq. (2) is obtained from eq. (1) by replacing $\boldsymbol{\theta}$ in $\mathbf{f}_1$ and $\mathbf{f}_2$ with the 6×6 identity matrix $\mathbf{I}_6$. The resulting solution matrix $\mathbf{W}$ has six columns yielding the solution for each of the six unit load vectors. Consequently, the solution to eq. (1) can be obtained as $\mathbf{w} = \mathbf{W}\boldsymbol{\theta}$, i.e., as the linear combination of the rows of $\mathbf{W}$ for any given $\boldsymbol{\theta}$. Consequently, the cross section compliance matrix $\mathbf{F}_s$ is given by

$$\mathbf{F}_s = \mathbf{W}^T \mathbf{G} \mathbf{W} \tag{3}$$

where matrix $\mathbf{G}$ is defined in Blasques and Stolpe [5]. For most practical applications $\mathbf{F}_s$ is symmetric positive definite and thus the cross section stiffness matrix is finally obtained from $\mathbf{K}_s = \mathbf{F}_s^{-1}$.

2.2. Beam finite element analysis

The cross section stiffness properties provided in the previous section are now integrated to generate the beam finite element stiffness matrices. The beam finite element static equilibrium equations yielding the nodal translations

and rotations $\hat{\mathbf{u}}$ for a given structure subjected to external loads $\hat{\mathbf{f}}$ is given by (cf. Bathe [3])

$$\hat{\mathbf{K}}\hat{\mathbf{u}} = \hat{\mathbf{f}} \quad \text{where} \quad \hat{\mathbf{K}} = \sum_{e=1}^{n_b} \hat{\mathbf{K}}_e = \sum_{e=1}^{n_b} \int_0^{L_e} \hat{\mathbf{B}}_e^T \mathbf{K}_s \hat{\mathbf{B}}_e \, dz \tag{4}$$

where n_b is the number of elements in the beam finite element assembly, L_e is the length of element e, and the summation refers to the typical finite element assembly. The beam finite element stiffness matrix $\hat{\mathbf{K}}_e$ is given in function of the cross section stiffness matrix $\mathbf{K}_s$ and the strain-displacement matrix $\hat{\mathbf{B}}_e = \mathcal{B}(\hat{\mathbf{N}}_e)$, where $\mathcal{B}$ is the strain-displacement relation and $\hat{\mathbf{N}}_e$ is the finite element shape function matrix. Herein, four node beam finite elements with cubic Lagrangean polynomials for interpolation functions are used. Each node has six degrees of freedom – three translations and three rotations.

2.3. Remarks

The application of the previously described methodology can be illustrated for, e.g., aeroelastic analysis of wind turbine blades. Wind turbine aeroelastic simulation tools often use beam finite elements to represent the blades of the turbine (see, .e.g., Larsen and Hansen [13]). In this context, the stiffness parameters in $\mathbf{K}_s$ can be efficiently and accurately determined to derive high-fidelity beam finite element models to represent the blades (cf., e.g, Kim et al. [11]). The instantaneous cross section forces and moments at a given section of the blade $\theta(t)$ can be retrieved from the aeroelastic simulations. The solutions $\mathbf{w}(t)$ can then be efficiently obtained as $\mathbf{w}(t) = \mathbf{W}\theta(t)$. Based on $\mathbf{w}(t)$ it is possible, among other, to obtain accurate estimates of instantaneous strains and stresses or, as described in the next section, the ERR associated with a longitudinal crack.

3. Fracture analysis

The previously described beam model is now employed in the analysis of the energy release rate (ERR) in cracked beams using the Virtual Crack Closure Technique (VCCT). The VCCT formulas based on 3D finite element models are presented first for reference. The formulas are subsequently adapted to use the results from the cross section equilibrium equations. Finally, other fracture mechanics concepts are introduced which will be used during the validation work presented in Section 4.

3.1. Virtual crack closure technique – VCCT

Assume that the static equilibrium equations $\overline{\mathbf{K}}\overline{\mathbf{u}} = \overline{\mathbf{f}}$ for a given 3D solid finite element assembly have been solved. Herein, $\overline{\mathbf{K}}$, $\overline{\mathbf{u}}$, and $\overline{\mathbf{f}}$ are the stiffness matrix, displacement vector, and load vector associated with the 3D solid finite element assembly, respectively. Assume also that the element reaction forces $\overline{\mathbf{r}}_e = \overline{\mathbf{K}}_e\overline{\mathbf{u}}_e$, $\forall e = 1, ..., n_s$ have been determined, where n_s is the number of elements in the assembly. Furthermore, the nodal reaction forces and displacements at any node of a given element e in the assembly are subsets of $\overline{\mathbf{r}}_e$ and $\overline{\mathbf{u}}_e$. Finally, consider a detail, cf. Fig. 4, of the same model including a crack where the ERR is to be determined. The crack coordinate system is defined as a local right-hand coordinate system with its origin at the crack tip. The x_1, x_3 -axes are aligned with the crack plane where the x_1-axis points into the designated crack extension direction. According to Krueger [12] the ERRs at the crack tip using 3D eight node solid finite elements with different length at the crack tip, i.e., $a_1 \neq a_2$, are obtained as

$$G_I = \frac{1}{2a_1c}\overline{r}_i^2\Delta\overline{u}_{j,k}^2, \quad G_{II} = \frac{1}{2a_1c}\overline{r}_i^1\Delta\overline{u}_{j,k}^1, \quad G_{III} = \frac{1}{2a_1c}\overline{r}_i^3\Delta\overline{u}_{j,k}^3 \tag{5}$$

where c is the crack width. According to the VCCT principle the nodal reaction forces $\overline{\mathbf{r}}_i = \begin{bmatrix} \overline{r}_i^1 & \overline{r}_i^2 & \overline{r}_i^3 \end{bmatrix}$ at node i multiply the relative displacements $\Delta\overline{\mathbf{u}}_{j,k} = \overline{\mathbf{u}}_j - \overline{\mathbf{u}}_k$ where $\overline{\mathbf{u}}_j = \begin{bmatrix} \overline{u}_j^1 & \overline{u}_j^2 & \overline{u}_j^3 \end{bmatrix}$ and $\overline{\mathbf{u}}_k = \begin{bmatrix} \overline{u}_k^1 & \overline{u}_k^2 & \overline{u}_k^3 \end{bmatrix}$ are the displacements of node j and k, respectively. Note that $\overline{\mathbf{r}}_i$ is obtained from the sum of the nodal reaction forces evaluated at each of the four elements associated with node i situated in the negative x_2 side of the x_1, x_3 plane. The previous quantities are defined in the crack coordinate system (x_1, x_2, x_3). The equivalent formulation using higher order elements can be found in Krueger [12].
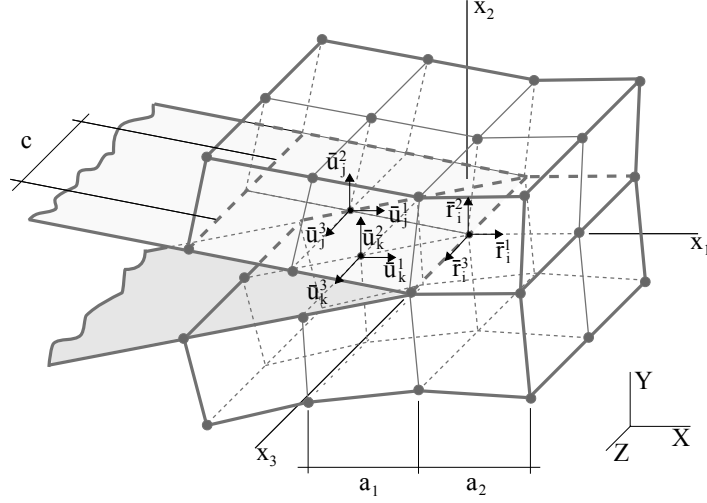
Figure 4: VCCT using 8 node solid finite elements (cf. Krueger [12]). The nodal forces $\bar{\mathbf{r}}_i = \left[\bar{r}_i^1 \ \bar{r}_i^2 \ \bar{r}_i^3\right]$ at node i are multiplied by the relative displacements $\Delta\bar{\mathbf{u}}_{j,k} = \bar{\mathbf{u}}_j - \bar{\mathbf{u}}_k$ where $\bar{\mathbf{u}}_j = \left[\bar{u}_j^1 \ \bar{u}_j^2 \ \bar{u}_j^3\right]$ and $\bar{\mathbf{u}}_k = \left[\bar{u}_k^1 \ \bar{u}_k^2 \ \bar{u}_k^3\right]$ are the displacements of node j and k, respectively. The crack coordinate system is defined by (x_1,x_2,x_3), whereas the global coordinate system is defined by (X, Y, Z).

3.2. VCCT in BECAS

The expressions for 3D solid finite elements in eq. (5) are now adapted to use the results from the beam model presented in Section 2. It is assumed at this point that the beam finite element equilibrium equations in eq. (4) have been solved. The internal forces at each element e of the beam finite element assembly are then given by $\hat{\mathbf{r}}_e = \hat{\mathbf{K}}_e\hat{\mathbf{u}}_e$. The cross section forces and moments θ at any position along the beam element can be determined through interpolation of the nodal values of $\hat{\mathbf{r}}_e$. Note that for statically determined structures the distribution of cross section forces and moments along the beam can be easily determined from analytical calculations. It is also assumed that the cross section equilibrium equations in eq. (2) have been previously solved such that $\mathbf{W}$ is known. The cross section generalized strains and curvatures ψ and 3D warping displacements $\mathbf{u}$ at each node of the cross section finite element mesh are then obtained from the relation $\mathbf{w} = \mathbf{W}\theta$. The nodal reaction forces $\mathbf{r}_e$ at an element e of the cross section finite element mesh are finally given as $\mathbf{r}_e = \mathbf{K}_e\mathbf{w}_e$, where $\mathbf{K}_e$ and $\mathbf{w}_e$ are the components associated with element e of $\mathbf{K}$ and $\mathbf{w}$, respectively.

Recall that the total displacement of any point in the cross section is described as the sum of the displacements associated with the rigid body translations and rotations, and the warping displacements. Note however that the rigid body motions do not induce relative displacements at the crack tip. Hence only the warping displacements $\mathbf{u}_e$ and corresponding components of $\mathbf{r}_e$ need to be taken into account for the evaluation of the ERR at crack the tip. The components of displacement and force necessary for the VCCT calculations are described in Fig. 5 for the linear Q4 and quadratic Q8 elements. The components of the ERR determined using Q4 elements are given by (cf. Fig. 5(a))

$$G_I = \frac{1}{2a_1}r_i^2\Delta u_{j,k}^2, \quad G_{II} = \frac{1}{2a_1}r_i^1\Delta u_{j,k}^1, \quad G_{III} = \frac{1}{2a_1}r_i^3\Delta u_{j,k}^3 . \tag{6}$$

Similarly to the 3D case, the relative displacements $\Delta\mathbf{u}_{j,k} = \mathbf{u}_j - \mathbf{u}_k$ where $\mathbf{u}_j = \left[u_j^1 \ u_j^2 \ u_j^3\right]$ and $\mathbf{u}_k = \left[u_k^1 \ u_k^2 \ u_k^3\right]$ are the nodal warping displacements of node j and k, respectively. The nodal forces at the crack tip of node i associated with the warping displacements $\mathbf{u}_i$ are given in $\mathbf{r}_i = \left[r_i^1 \ r_i^2 \ r_i^3\right]$. Also like in the 3D case, $\mathbf{r}_i$ are sum of the nodal reaction forces evaluated at each of the two elements associated with node i situated in the negative x_2 side of the x_1, x_3 plane. All previous quantities are defined in the crack coordinate system (x_1,x_2,x_3). For ERR computations
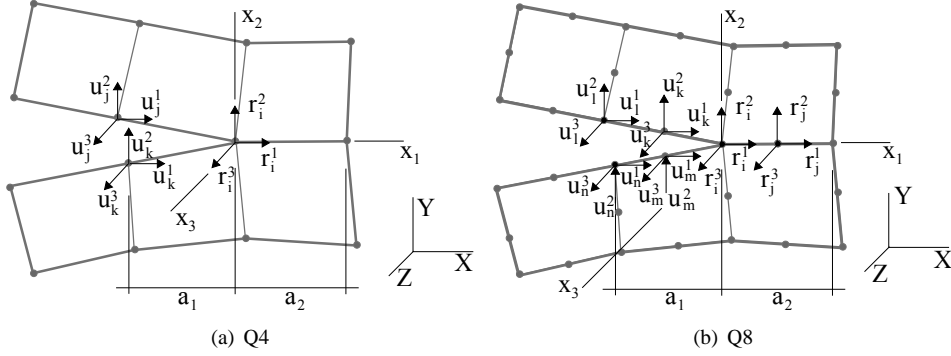
Figure 5: VCCT within the cross section finite element mesh in BECAS. (a) Using the Q4 linear element, the nodal forces $\mathbf{r}^i = \begin{bmatrix} r_1^i & r_2^i & r_3^i \end{bmatrix}$ at node i are multiplied by the relative displacements $\Delta\mathbf{u}_{j,k} = \mathbf{u}_j - \mathbf{u}_k$, where $\mathbf{u}^j = \begin{bmatrix} u_1^j & u_2^j & u_3^j \end{bmatrix}$ and $\mathbf{u}^k = \begin{bmatrix} u_1^k & u_2^k & u_3^k \end{bmatrix}$ are the displacements of node j and k, respectively. (b) Using the Q8 quadratic element the nodal forces $\mathbf{r}^i = \begin{bmatrix} r_1^i & r_2^i & r_3^i \end{bmatrix}$ and $\mathbf{r}^j = \begin{bmatrix} r_1^j & r_2^j & r_3^j \end{bmatrix}$ at node i and j, respectively, are multiplied by the relative displacements $\Delta\mathbf{u}_{l,n} = \mathbf{u}_l - \mathbf{u}_n$ of node l and n and $\Delta\mathbf{u}_{k,m} = \mathbf{u}_k - \mathbf{u}_m$ of node k and m, respectively. Note that the two-dimensional finite elements have three displacements per node in order to approximate the in- and out-of-plane deformation of the cross section. The crack coordinate system is defined by (x_1, x_2, x_3), whereas the global coordinate system is defined by (X, Y, Z).

using Q8 elements the expressions are (cf. Fig. 5(b))

$$G_I = \frac{1}{2a_1}\left[r_i^2 \Delta u_{l,n}^2 + r_j^2 \Delta u_{k,m}^2 \right], \; G_{II} = \frac{1}{2a_1}\left[r_i^1 \Delta u_{l,n}^1 + r_j^1 \Delta u_{k,m}^1 \right], \tag{7}$$

$$G_{III} = \frac{1}{2a_1}\left[r_i^3 \Delta u_{l,n}^3 + r_j^3 \Delta u_{k,m}^3 \right] \tag{8}$$

where $\Delta\mathbf{u}_{l,n} = \mathbf{u}_l - \mathbf{u}_n$ and $\Delta\mathbf{u}_{k,m} = \mathbf{u}_k - \mathbf{u}_m$. The notation is the same as before so further details are omitted for brevity. Due to the two dimensional character of the beam and cross section analysis formulation, $c = 1$ in eq. (6) and (8).

Finally, note that although the analysis is based on a 2D finite element discretization of the cross section, all 3D components of the displacements at each node of the cross section finite element mesh are evaluated. As a consequence it is possible to compute the ERR associated with mode III crack opening.

3.3. Other methods and concepts

This section briefly describes other fracture mechanics methods and concepts which will be invoked throughout the validation work in Section 4.

3.3.1. Contour integration

A prominent way to obtain the ERR in linear elastic fracture mechanics is the well known J-integral originally proposed by Rice [19] and further discussed by Budiansky and Rice [7]. In this paper J-integral based calculations of the ERR using 3D finite element models are included in order to obtain additional reference values which are independent of the assumptions underlying the analytical solutions or the VCCT. It should be noted that the J-integral only yields the total energy release rate G_{tot} and does not provide the modal contributions G_I, G_{II} and G_{III}.

3.3.2. Analytical solutions

Analytical solutions for stress intensity factors of cracks in linear elastic single material cases can be found in Murakami [14]. Two of the results are presented here which will be used in Section 4.2 for validation. The analytical solution for the Mode-III stress intensity factor for a cylindrical beam with a radial crack (see Fig. 6(a)) subjected to a torsional moment M_z is given as

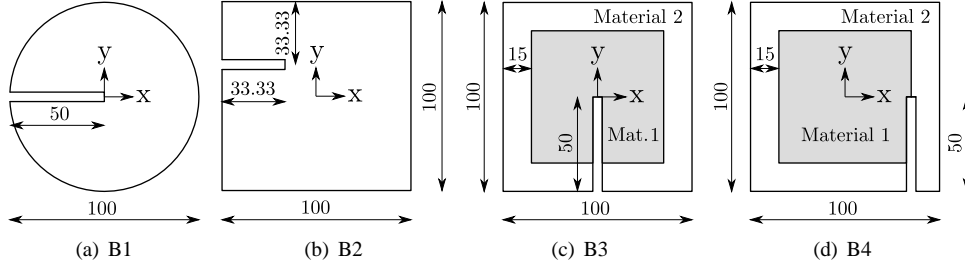$$K_{III} = \frac{-0.969274 \, M_z}{a^{2.5}} \tag{9}$$

8

Figure 6: Dimensions, material distribution, and cross section coordinate system of the four beam cross sections considered in this study. All dimensions in [mm]. (a) Circular beam with radial crack, (b) square beam with eccentric edge crack, (c) bi-material square beam with centered edge crack, and (d) bi-material square beam with crack at the material interface.

where a is the crack length. The solution for the same beam subject to a shear force T_y is given as

$$K_{III} = \frac{(1.375776 + 1.354244\nu)\, T_y}{(1+\nu)\, a^{1.5}} \tag{10}$$

where ν is Poisson's ratio. The solution for a single edge cracked square beam (see Fig. 6(b)) subjected to a torsional moment M_z is

$$K_{III} = \frac{3.22482\, M_z}{W^{2.5}} \tag{11}$$

where W is the cross section width. The constants used in these equations are based on the geometrical properties of the cases presented in Section 4.2. The Mode-III ERR of both aforementioned cases can be obtained from

$$G_{III} = \frac{(1+\nu)\, K_{III}^2}{E} \tag{12}$$

where E is the Young's modulus.

3.3.3. Bi-material interfaces

For problems featuring a crack at the interface between two linear elastic, isotropic materials the asymptotic solution for the near crack tip stress field oscillates with increasing amplitude and frequency when approaching the crack tip – the so-called "oscillating singularity". The analytical asymptotic solution for the near crack tip stress field depends on the four elastic constants only through the bi-material constant η defined as

$$\eta = \frac{1}{2\pi} \ln\left(\frac{1+\beta}{1-\beta}\right), \quad \beta = \frac{(\mu_2/\mu_1)\,(\kappa_1 - 1) - (\kappa_2 - 1)}{(\mu_2/\mu_1)\,(\kappa_1 + 1) + (\kappa_2 + 1)}, \quad \kappa_i = \frac{3 - \nu_i}{1 + \nu_i} \tag{13}$$

where β is the second Dundurs parameter and κ_i is a material constant for generalized plane stress (Bogy [6], Dundurs [8]). μ_1 and μ_2 are the shear moduli and ν_1 and ν_2 are the Poisson's ratios of material 1 and 2, respectively. The mode mixity angle ψ, defining the ratio of shear to normal traction at the interface, can also be written as

$$\psi = \arctan \sqrt{\frac{G_{II}}{G_I}} \, . \tag{14}$$

The asymptotic solution near the crack tip yields

$$\psi = \varphi + \eta \ln(r) \tag{15}$$

where r is the distance from the crack tip and φ is a constant. Note that the mode mixity ψ depends on the distance from the crack tip r and is not defined for $r \to 0$. That is, interface cracks are inherently mixed mode. The value of ψ at a fixed distance $r = L_0$ is commonly used as a measure of the mode mix (O'Dowd [15]). Equation (15) also applies to the mode mixity predicted by the VCCT, if r is replaced by the width of the element next to the crack tip a. Results independent of the element size can then be obtained by evaluating eq. (15) at a fixed distance L_0 from the crack tip.

9

Table 1: Young's modulus (E_α), Poisson's ratio (ν_α), number of finite elements (# elem) in the cross section mesh, and near crack tip element size (Δa) for all numerical experiments (cf. Figure 6). Three different mesh resolutions – coarse, medium, and fine – are considered for case B4.

Case	E_1	E_2	ν_1	ν_2	# elem.			Δ a		
	[Pa]	[Pa]	-	-	-			[mm]		
B1	7×10^{10}	-	0.28	-	880			2.0		
B2	7×10^{10}	-	0.28	-	900			3.33		
B3	2×10^{10}	2×10^{11}	0.45	0.0	784			3.5		
					coarse	medium	fine	coarse	medium	fine
B4	2×10^{10}	2×10^{11}	0.45	0.0	784	1444	3364	3.4	2.01	1.1

(a) Case B1, load case f_y (b) Case B2, load case m_z (c) Case B3, load case f_y (d) Case B4, load case m_x
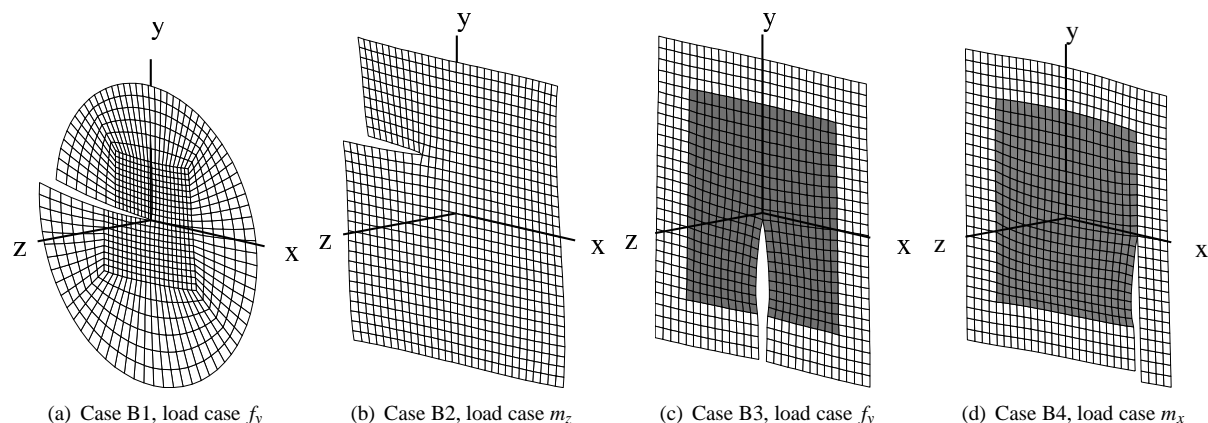
Figure 7: Cross section finite element mesh and warping deformation for selected load cases for the beams considered in the study (cf. Fig. 6). Note that (d) shows the coarse mesh. The magnitude of the loads is indicated in Table 2. Deformation is scaled for visualization.

4. Numerical experiments

This section describes the setup and presents validation results for a series of numerical examples. The ERR evaluated using the proposed approach are compared with analytical solutions and results from detailed three-dimensional finite element models.

4.1. Setup

Four straight cantilever beams of constant cross section with a length of 2.0 m were considered. All cross sections feature a single crack that extends along the length of the beam. The geometrical dimensions and material distribution for each of the beams are schematically described in Fig. 6. Table 1 indicates the mechanical properties of the materials, number of elements in the cross section finite element mesh, and the element size near the crack tip for each cross section. The beams were loaded by either forces or moments applied at the free end. The load cases considered for each of the numerical experiments are presented in Table 2. The magnitudes of the loads were chosen such that the magnitudes of the von Mises stresses at midspan are similar for the different load cases. The 2D finite element mesh used in BECAS for each of the cross sections is shown in Fig. 7. The near tip element length in the cracked part a_1 and in the uncracked part a_2 were chosen to be equal, i.e., $a = a_1 = a_2$ for all cases. In BECAS both linear four node elements Q4 and quadratic eight node elements Q8 were used.

Beam B1 in Fig. 6(a) corresponds to a single material beam with circular cross section and a radial crack that extends to its centre. Beam B2 in Fig. 6(b) is a single material beam with square cross section and an eccentric edge crack. The cross section finite element mesh for both cases is presented in Figures 7(a) and 7(b). For these two cases – B1 and B2 – analytical solutions exist for the ERR as given in Section 3.3.2. Figure 6(c) shows the cross section geometry and material distribution for the bi-material square beam with a centered crack – beam B3. The cross section finite element mesh is presented in Fig. 7(c). The beam is composed of a soft and almost incompressible core material – Material 1 – and a compressible and stiff material distributed on the outside – Material 2. The crack tip is located in

10

Table 2: Forces – f_x, f_y, and f_z – and moments – m_x, m_y, and m_z – considered for each of the four numerical experiments (cf. Fig. 6). All loads are applied at the free-end of the beam finite element model individually.

Load case	f_x [N]	f_y [N]	f_z [N]	m_x [Nm]	m_y [Nm]	m_z [Nm]
B1	–	1×10^4	–	–	–	1.0×10^4
B2	–	–	–	–	–	-1.0×10^4
B3	2.0×10^4	2.0×10^4	6.0×10^5	-2.0×10^4	2.0×10^4	5.0×10^3
B4	–	–	-6.0×10^6	–	–	5.2×10^4

the core material. Finally, Fig. 6(d) shows the same bi-material square beam cross section although the crack plane is now placed at the interface between outer rim and core – beam B4. The same material properties as used for beam B3 were adopted. This model was analysed for three different mesh discretisation levels and near crack tip element sizes hereafter referred to as *coarse*, *medium* and *fine* mesh. The coarse mesh is depicted in Fig. 7(d).

The 3D solid finite element models used in the validation were built and analyzed in ABAQUS [1] using 8 node solid incompatible mode elements (ABAQUS element type C3D8I). The models were discretised using 61 elements in the axial z direction for both the VCCT and contour integration analysis. For VCCT calculations the 3D solid finite element models were extruded versions of the 2D meshes used in BECAS. For the contour integration a fine mesh was chosen with circular concentric element rings around the crack tip each consisting of 12 elements. In ABAQUS, the J-integral is calculated by integration along a circular array of elements around the crack tip. For this purpose the contour integral formulation is reformulated into a domain integral. The ERR was evaluated along the third ring of elements.

Currently BECAS cannot account for effects stemming from contact of the crack faces. Consequently, the presented examples were designed to avoid interpenetration of the crack faces and thus ensure that the results are physically meaningful.

An important motivation for using the BECAS VCCT approach instead of a standard 3D finite element model for fracture analysis is computational efficiency. Hence, the computational time required by the BECAS VCCT approach for the bi-material square beam with crack at the material interface B4 (Fig. 6 (d)) was compared with the corresponding 3D finite element model. Three different discretization levels were used for the 2D cross section mesh employing linear Q4 elements. The 3D finite element models were those used for the VCCT calculations as described earlier in this section. The 3D finite element analyses were performed in ABAQUS [1] and comprised a single, linear static analysis procedure using the default direct sparse solver. Both, the ABAQUS and the BECAS analysis, were executed on a single CPU of a Dell PowerEdge R410 with two Intel Xeon X5650 six-core CPUs at 2.66 GHz and 24 GB memory.

4.2. Results

Five different types of results are referred to throughout the next sections. BECAS VCCT Q4 and BECAS VCCT Q8 refer to the cases where the ERR was computed using the VCCT based on linear Q4 and quadratic Q8 elements in BECAS, respectively. 3D FE VCCT and 3D FE J-int. refers to the cases where the results were computed using the VCCT and contour integration techniques within a 3D finite element model, respectively. Finally, the "analytical" results refer to the results that were calculated using the analytical expressions presented in Section 3.3.2.

All ERR results presented in Tables 3 through 5 refer to values evaluated at a section situated at midspan, i.e., at 1.0 m. The aim was to minimize the influence of effects stemming from the boundary conditions enforced at the beam ends for each of the different modeling approaches. Henceforth the relative difference d_r between two quantities A and B in percent is defined as $d_r = |1 - A/B| \times 100$.

The ERR values obtained for beam B1 – circular beam with radial crack – and B2 – square beam with eccentric edge crack – using the VCCT in BECAS are presented in Table 3. The load cases – f_y and m_z – are those for which analytical results were available. Results from BECAS were obtained using linear four node Q4 elements and quadratic eight node Q8 elements. The results are compared with the analytical solutions given in eqs. (10) through (12). Moreover, the contour integration (3D FE J-int.) and VCCT (3D FE VCCT) calculations performed using a 3D solid finite element model are presented for reference. The relative difference is given with respect to the analytical results.

Table 3: Energy release rates for beam B1 and B2 (cf. Fig. 6). Load cases according to Table 2. *Analytical* values are given by eq. (10 - 12). The *BECAS Q4 VCCT* and *BECAS Q8 VCCT* refer to results obtained using VCCT within the cross section analysis tool BECAS with four and eight node plane finite elements, respectively. The *3D FE J-Int.* and *3D FE VCCT* refer to numerical results obtained using contour integration and VCCT within a three-dimensional solid finite element model, respectively. The relative difference (*Rel. Err.*) reflects the deviation between the values predicted by numerical simulations and the analytical solutions.

Case	B1 (Circular)				B2 (Square)	
Load case	m_z		f_y		m_z	
	G_{III}	Rel. Err.	G_{III}	Rel. Err.	G_{III}	Rel. Err.
Method	[J/m^2]	[%]	[J/m^2]	[%]	[J/m^2]	[%]
Analytical	5497	-	27.50	-	1902	-
BECAS Q4 VCCT	5479	0.3	26.99	1.9	1904	0.1
BECAS Q8 VCCT	5481	0.3	27.24	0.9	1920	1.0
3D FE J-Int.	5607	2.0	28.26	2.8	1921	1.0
3D FE VCCT	5468	0.5	26.97	1.9	1904	0.1

Table 4: Energy release rates for the beam B3 (cf. Fig. 6). Load cases according to Table 2. The *BECAS Q4 VCCT* refers to results obtained using VCCT within the cross section analysis tool BECAS with four node plane finite elements. The *3D FE J-Int.* and *3D FE VCCT* refer to numerical results obtained using contour integration and VCCT within a three-dimensional solid finite element model, respectively. The relative difference (*Rel. Err.*) reflects the deviation between the values predicted by *3D FE VCCT* and *BECAS Q4 VCCT*, and the results obtained using *3D FE J-Int.*.

Method	Load case		f_x	f_y	f_z	m_x	m_y	m_z
3D FE J-Int.	G_{tot}	[J/m^2]	167.2	22.3	20.7	21.7	10.5	1070.1
	G_I	[J/m^2]	0.0	21.0	21.0	21.0	0.0	0.0
	G_{II}	[J/m^2]	10.2	0.0	0.0	0.0	10.2	0.0
BECAS Q4	G_{III}	[J/m^2]	155.0	0.0	0.0	0.0	0.0	1064.2
VCCT	G_{tot}	[J/m^2]	165.2	21.0	21.0	21.0	10.2	1064.2
	Rel. Err.	[%]	1.2	5.6	1.4	3.3	3.1	0.6
	G_I	[J/m^2]	0.0	20.9	20.5	20.9	0.0	0.0
	G_{II}	[J/m^2]	10.3	0.0	0.0	0.0	10.3	0.0
3D FE	G_{III}	[J/m^2]	155.9	0.0	0.0	0.0	0.0	1064.6
VCCT	G_{tot}	[J/m^2]	166.1	20.9	20.5	20.9	10.3	1064.6
	Rel. Err.	[%]	0.6	6.0	1.3	3.7	1.8	0.5

Table 5: Element size independent energy release rates for beam B4 (cf. Fig. 6) evaluated at a distance $L_0 = 0.1$mm (cf. Fig. 8). Load cases according to Table 2. The *BECAS Q4 VCCT* refers to results obtained using VCCT within the cross section analysis tool BECAS with four node plane finite elements Q4. The *3D FE J-Int.* and *3D FE VCCT* refer to numerical results obtained using contour integration and VCCT within a three-dimensional solid finite element model, respectively. The relative difference (*Rel. Err.*) reflects the deviation between *3D FE VCCT* and *BECAS Q4 VCCT* for three different finite element mesh discretizations (cf. Table 1), and the values predicted by *3D FE J-Int.*.

| Method	Load case		f_z			m_z		
3D FE J-Int.	G_{tot}	[J/m^2]	5152			44545		
			Coarse	Medium	Fine	Coarse	Medium	Fine
	G_I	[J/m^2]	2787	2767	2793	0	0	0
	G_{II}	[J/m^2]	2646	2605	2545	0	0	0
BECAS Q4	G_{III}	[J/m^2]	0	0	0	44505	44559	44567
VCCT	G_{tot}	[J/m^2]	5433	5371	5338	44505	44559	44567
	Rel. Err.	[%]	5.5	4.3	3.6	0.1	0.0	0.1
	G_I	[J/m^2]	2547	2475	2473	0	0	0
	G_{II}	[J/m^2]	2715	2753	2731	0	0	0
3D FE	G_{III}	[J/m^2]	0	0	0	44505	44570	44570
VCCT	G_{tot}	[J/m^2]	5262	5228	5204	44505	44570	44570
	Rel. Err.	[%]	2.1	1.5	1	0.1	0.1	0.1
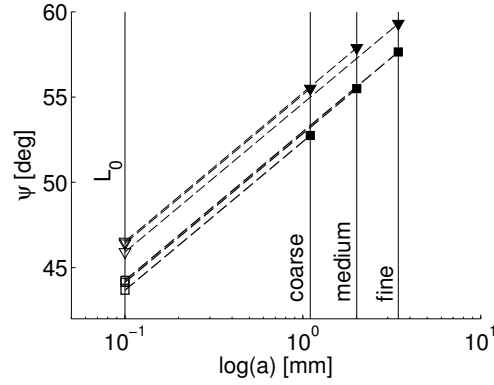
Figure 8: Mode mixity ψ as a function of element size a for the bi-material square beam with crack at the material interface B4. Square and triangle markers refer to BECAS and 3D FE results, respectively. Solid markers are results obtained from VCCT. Hollow markers are the corresponding element size independent results for an evaluation distance $L_0 = 0.1$mm.
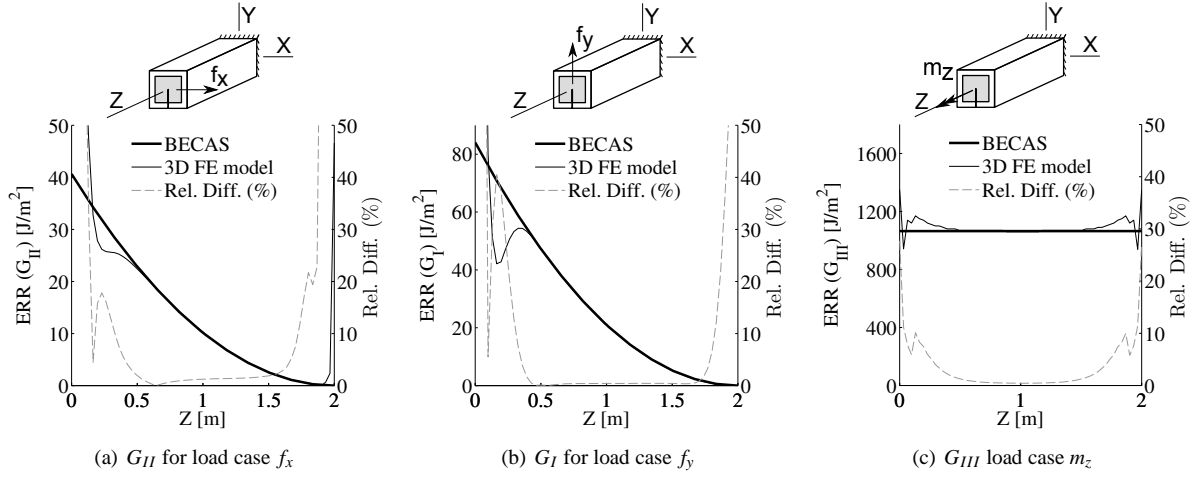

(a) G_{II} for load case f_x

(b) G_I for load case f_y

(c) G_{III} load case m_z

Figure 9: Selected results showing the variation of the strain energy release rates along the lengthwise direction z for beam B3 (see Fig. 6) for different load cases (see Table 2). Values computed using VCCT within the beam finite element model based on the cross section analysis tool BECAS, and 3D solid finite element model in ABAQUS. The origin of the coordinate system is at the clamped end of the beam.

The resulting ERR values for beam B3 – bi-material square beam with centered crack – are presented in Table 4 for six different load cases – f_x, f_y, f_z, m_x, m_y, and m_z. This combination of material lay-out and load cases makes it possible to trigger and compare each ERR component individually. The ERR results for beam B4 – bi-material square beam with crack at the material interface for two load cases – f_z and m_z – and three different mesh refinements are presented in Table 5. The results in this table were made element size independent using an evaluation distance of $L_0 = 0.1$ mm as explained in Section 3.3.3 and illustrated in Fig. 8. In both Table 4 and 5 the ERR obtained using VCCT in BECAS and the 3D finite element model for each of the different fracture modes – G_I, G_{II}, and G_{III} – are presented for comparison. The total ERR values G_{tot} obtained using VCCT in both BECAS and 3D finite element model are compared against the values computed using contour integration in the 3D solid finite element model.

The variation of the ERR measured along the length of the beam is analysed in Fig. 9. Illustrative results obtained using VCCT in BECAS and 3D finite element models are presented for beam B3 for selected load cases.

Finally, Table 6 lists the number of degrees of freedom and the total execution time for the BECAS and 3D finite element models of beam B4. It can be observed that the BECAS models execute between 50 times (coarse mesh) and 173 times (fine mesh) faster than the corresponding ABAQUS models.

Table 6: Total computation time (assembly and solution) for computation of energy release rate using VCCT within the cross section analysis tool BECAS and three-dimensional finite element model in ABAQUS. Three different finite element mesh discretizations are considered cf. Table 1.

| Mesh density | BECAS | | 3D FE | |
| | Degrees of freedom | CPU time | Degrees of freedom | CPU time |
-		[s]		[s]
Coarse	2.565×10^3	1.34	1.590×10^5	67.52
Medium	4.620×10^3	2.24	2.864×10^5	177.10
Fine	1.053×10^4	4.95	6.529×10^5	858.60

5. Discussion

In the B1 and B2 cases, the results (see Table 3) computed using BECAS agree very well with the analytical results, the largest relative difference being 1.9%. Note also that the relative differences between the 3D FE (VCCT and J-int.) and analytical values is of the same order.

Results for the bi-material square beam with centered crack B3 show that the G_{tot} values agree well, the largest relative difference being 5.6% (see Table 4). The values are within the same range as the results obtained based on the 3D FE VCCT. Evaluating the relative differences between the individual components G_I, G_{II} and G_{III} from BECAS VCCT and the 3D FE VCCT shows that the results are in even better agreement. In this case the largest relative difference between each of the values is 2.8%. The BECAS VCCT results for beam B3 were also obtained using quadratic eight node elements (Q8). In this case the maximum relative difference between BECAS VCCT and 3D FE VCCT for each of the individual components was 1.6%. These results are omitted for brevity.

Unlike the previous examples, the crack in beam B4 was placed at the interface between two materials. From Table 5 it is visible that the results agree well with the 3D FE J int. in terms of the total energy release rate, the largest relative difference being 5.5%. In this case the relative error values are slightly larger than those resulting from the comparison between the 3D FE VCCT and the 3D FE J-int. Comparing the BECAS VCCT and 3D FE VCCT results for each individual component G_I, G_{II} and G_{III} yields a maximum relative error of 13%. However, comparing the total energy release rates G_{tot} results in a maximum relative difference of only 3.2%. Moreover, the mode mixity angle ψ for this two cases – BECAS VCCT and 3D FE VCCT – also agrees very well with the largest absolute difference being 2.7°. The relatively small difference in mode mixity angles can also be observed in Figure 8.

The proposed beam model allows for the precise definition of the warping displacements – the only contribution to crack deformation – in terms of the cross section forces and moments. Consequently it is possible to gain an insight into the relation between the beam and cross section loading and the different ERR components. The deformed shape considering only the warping displacements is presented in Figure 7 for each of the cross sections. For the load cases considered in case B1 and B2, G_{III} is the only non-zero component of the ERR. The mode III crack opening visible in Fig. 7(a) and 7(b) is a result of the out-of-plane warping deformation induced by the transverse forces and torsional moment at the cross section of interest, respectively. It was further observed that in these cases – B1 and B2 – the in-plane warping displacements resulting from the bending moment induced by the tip loading do not induce mode I or II deformation which explains why G_I and G_{II} are null. In the case of beam B3 note that the ERR values for load case f_y and m_x are the same. This is due to the fact that the mode I crack opening depicted in Fig. 7(c) is a function of the in-plane warping displacements induced by the cross section bending moment M_x only, which is the same in both load cases. Finally, unlike the cases of beam B1 and B2, in beam B4 the bending moment will induce deformation at the crack tip (see Fig. 7(d)) as a result of the interaction between the two materials.

All results in Tables 3 through 5 refer to the beam mid-section values at $z = 1$ m. The variation of the strain energy release rates along the length direction z are presented Fig. 9. The results are for beam B3 as computed by BECAS VCCT and 3D FE VCCT where the relative difference is computed using the 3D FE results as reference values. The quadratic lengthwise variation of the ERR in Fig. 9 (a) and (b) is a result of the linear lengthwise variation of the bending moment induced by the transverse tips loads f_x and f_y, respectively. The constant ERR value in Fig. 9 (c) is a consequence of the constant torsional moment induced by the torque applied at the tip of the beam. For all three cases there is a good agreement between the ERR results from BECAS VCCT and 3D FE VCCT in the central region of the beam. However, the results present considerable deviations closer to the ends of the beam where the loads and clamped constraints are applied. This is a consequence of the different assumptions associated with the warping
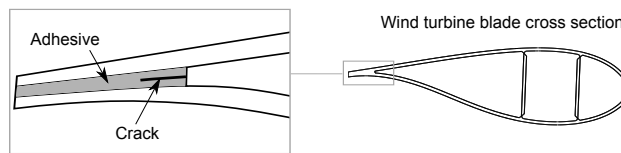
Figure 10: Schematic description of a crack in the trailing edge adhesive joint of a wind turbine rotor blade.

deformation at the ends of the beam in both models. The 3D FE model was conceived to approximate the free warping boundary conditions which are assumed in the proposed beam model. The boundary conditions (fixed end of the cantilever) and loads (free end of the cantilever) are applied in the 3D model using the so-called "distributing coupling constraints" [1]. In this case, nodal forces are distributed in such a way that the resultants of these forces are equivalent to the forces and moments at a specified reference node. Although this technique allows for warping deformation of the end sections it does not ensure that the 3D FE and BECAS warping fields are the same. The large variations in the results suggest that the ERR is very sensitive to the warping deformation. Future work will focus on further numerical experimentation to analyze the influence of beam slenderness and crack length in the decay length of the effects stemming from the boundary conditions. It is likely that an increase in beam slenderness and relatively smaller crack lengths will contribute to a decrease of the relative decay length of the boundary effects.

Illustrative results comparing the computation times used by BECAS and 3D FE are presented in Table 6. The CPU time refers to assembly and solution of the finite element equations. From the point of view of the 3D finite element model note that the comparison is not entirely consistent. Factors like the discretization in the axial direction, the element type, the equation solver, the adoption of sub-modeling techniques, or the use of parallel computing strategies, among other, will have an impact on the execution time. From the point of view of the BECAS model it should be noted that the execution times presented in Table 6 only hold for beams with constant cross section. Nevertheless, the data in Table 6 gives an indication that the BECAS VCCT approach is computationally very efficient. Moreover, while the memory usage of the different models was not investigated, it is evident based on the number of degrees of freedom that the BECAS VCCT models require considerably less memory.

The academic examples presented here illustrate the potential of the framework. Future work will focus on applying the proposed framework to the analysis of cracks and delaminations in wind turbine blades. Figure 10 shows an example of a crack in the trailing edge adhesive bond of a wind turbine blade. As the crack length is in the order of centimeters and the length of the largest existing blades is in the order of 80 meters, three dimensional finite element shell or solid models including the crack can be computationally expensive. If it is conservatively assumed that the crack has a large extension in the blade's lengthwise direction, the energy release rates at the crack tip can be computed very efficiently using the framework proposed in this paper.

6. Conclusions

A methodology has been presented for the efficient and accurate evaluation of energy release rates (ERR) in long and slender beam structures with longitudinal cracks. The structural response is analyzed based on a beam finite element model comprising a finite element based cross section analysis tool. The cross section analysis tool computes the cross section stiffness and mass properties while accounting for effects stemming from material inhomogeneity and anisotropy in beams with arbitrary section geometry. The ERR is determined based on an implementation of the Virtual Crack Closure Technique (VCCT) in the cross section analysis framework. A series of validation examples with different cross section geometries and material distributions, including a case with a crack at a bi-material interface, were analyzed. The ERR for modes I, II and III were compared against analytical values, and VCCT and contour integration results obtained from 3D solid finite element models. All results showed very good agreement. Furthermore, for the bi-material interface case the observed behavior matched well the expected behavior based on the asymptotic solution for the near crack tip stress field. Furthermore, the effect of the boundary conditions on the ERR values along the length of the beam were studied and their influence was established. Finally, it is shown that the devised methodology uses only a fraction of the computational time required by 3D finite element models.

In sum, the results suggest that the proposed framework can be used to efficiently and accurately compute the mode I, II, and III energy release rates in a general class of beam structures with longitudinal cracks. Consequently,

it is now possible to analyze a large number of model configurations (varying crack location, orientation and size) or instead consider levels of mesh refinement which are computationally prohibitive within 3D finite element models.

Future work will focus on the application of this methodology to the analysis wind turbine blades, namely, in the fatigue crack growth analysis of adhesive bonds.

Acknowledgements

References

[1] ABAQUS 6.11, 2011. Abaqus Analysis User's Manual. Dassault Systèmes.

[2] Barenblatt, G., 1962. The mathematical theory of equilibrium cracks in brittle fracture. Advances in Applied Mechanics 7, 55–129.

[3] Bathe, K. J., 1996. Finite Element Procedures. Prentice Hall, Englewood Cliffs – New Jersey.

[4] Blasques, J. P., 2014. Multi-material topology optimization of laminated composite beams with eigenfrequency constraints. Compos Struct 111, 45–55.

[5] Blasques, J. P., Stolpe, M., 2012. Multi-material topology optimization of laminated composite beam cross sections. Compos Struct 94 (11), 3278–3289.

[6] Bogy, D. B., 1968. Edge-bonded dissimilar orthogonal elastic wedges under normal and shear loading. J Appl Mech 35 (3), 460–466.

[7] Budiansky, B., Rice, J. R., 1973. Conservation laws and energy-release rates. J Appl Mech 40 (1), 201–203.

[8] Dundurs, J., 1969. Discussion of [6]. J Appl Mech 36 (3), 650–652.

[9] Eder, M., Bitsche, R., 2014. Fracture analysis of adhesive joints in wind turbine blades. Wind Energy.

[10] Giavotto, V., Borri, M., Mantegazza, P., Ghiringhelli, G., Carmaschi, V., Maffioli, G., Mussi, F., 1983. Anisotropic beam theory and applications. Comput Struct 16 (1-4), 403–413.

[11] Kim, T., Hansen, A., Branner, K., 2013. Development of an anisotropic beam finite element for composite wind turbine blades in multibody system. Renew Energ 59, 172–183.

[12] Krueger, R., 2004. Virtual crack closure technique: History, approach, and applications. Appl Mech Rev 57 (1-6), 109–143.

[13] Larsen, T. J., Hansen, A. M., 2007. How 2 HAWC2, the user's manual. Denmark. Forskningscenter Risø. Risø-R. Risø National Laboratory.

[14] Murakami, Y., 1987. Stress Intensity Factors Handbook. Vol. 2. Pergamon Press.

[15] O'Dowd, N. P., 2008. Concise Encyclopedia of the Properties of Materials Surfaces and Interfaces, chap. Fracture at Interfaces, 1st Edition. Elsevier.

[16] Overgaard, L., Lund, E., 2010. Structural collapse of a wind turbine blade. Part B: Progressive interlaminar failure models. Composites Part A: Applied Science and Manufacturing 41 (2), 271–283.

[17] Overgaard, L., Lund, E., Camanho, P., 2010. A methodology for the structural analysis of composite wind turbine blades under geometric and material induced instabilities. Computers & Structures 88 (19-20), 1092–1109.

[18] Overgaard, L., Lund, E., Thomsen, O., 2010. Structural collapse of a wind turbine blade. Part A: Static test and equivalent single layered models. Composites Part A: Applied Science and Manufacturing 41 (2), 257–270.

[19] Rice, J. R., 1968. A Path Independent Integral and the Approximate Analysis of Strain Concentration by Notches and Cracks. J Appl Mech 35 (2), 379–386.

[20] Rybicki, E. F., Kanninen, M. F., 1977. Finite-element calculation of stress intensity factors by a modified crack closure integral. Eng Fract Mech 9 (4), 931–938.

[21] Volovoi, V., Hodges, D., Cesnik, C., Popescu, B., 2001. Assessment of beam modeling methods for rotor blade applications. Mathematical and Computer Modelling 33 (10-11), 1099–1112.

[22] Xie, D., Waas, A., 2004. Computation of energy release rates for kinking cracks based on virtual crack closure technique. Computer Methods in Engineering Science 6 (6), 515–524.